

Slenderness Effect on GFRP-RC Columns with Square Spirals under Concentric and Eccentric loading: Experimental and Analytical Study

Alireza Sadat Hosseini^{1*} and Pedram Sadeghian²

¹ Research Assistant, Department of Civil and Resource Engineering, Dalhousie University, Canada

² Associate Professor and Canada Research Chair in Sustainable Infrastructure, Department of Civil and Resource Engineering, Dalhousie University, Canada

* Corresponding Author, email: asadat@dal.ca

ABSTRACT

This study investigates the behavior of slender glass fiber-reinforced polymer-reinforced concrete (GFRP-RC) columns, specifically those reinforced with GFRP bars and square spirals. Nine column specimens were tested, with varying slenderness ratios of 20, 40, and 60, and load eccentricities of 0%, 15%, and 30% of the section height. Under concentric loading, increased slenderness led to a 16-31% decrease in column strength, primarily due to amplified bending moments and lateral deformations, worsened by the asymmetry of the square spirals. Under eccentric loading, spiral rupture was observed only at a slenderness ratio of 20 and 15% eccentricity. Spirals provided critical stability for shorter columns under moderate loads, but their effectiveness diminished in more slender columns and under higher eccentricities. As slenderness increased, the spirals' contribution to confinement and load-bearing capacity decreased; for instance, at 15% eccentricity, increasing slenderness from 20 to 60 reduced load capacity by 13% and 32%, respectively. A transition in failure mode from compression-dominated to bending-dominated failure was observed as eccentricity increased. An analytical model, assuming sine-shaped deformation for single-curvature bending, was developed and validated against experimental data. Based on this, a slenderness limit of 14 for GFRP-RC columns with 2–4% longitudinal reinforcement ratio was recommended.

DOI: <https://doi.org/10.1016/j.engstruct.2025.120277>

Keywords: GFRP-Reinforcement; Concrete; Slender Column; Square Spiral; Load Eccentricity; Slenderness Limit

1. INTRODUCTION

Glass fiber-reinforced polymer (GFRP) reinforcement has emerged as a durable and corrosion-resistant alternative to traditional steel reinforcement in reinforced concrete (RC) structures, particularly in aggressive environments. Its advantages, including high corrosion resistance, lightweight properties, and ease of installation, make it an attractive option for marine infrastructure, bridges, and other structures exposed to harsh conditions. In square columns, GFRP square spirals, produced through the pultrusion process, serve as continuous transverse reinforcement, offering a more integrated system compared to discrete ties.

Slender columns are integral to modern structural applications, such as high-rise buildings, bridge piers, industrial facilities, and offshore platforms, where they efficiently support axial and lateral loads while minimizing material usage. The combination of GFRP reinforcement and slender column design presents significant potential for enhancing structural durability and performance. However, despite these advantages, the behavior of slender GFRP-RC columns under varying loading conditions, particularly under concentric and eccentric loads, remains an area requiring further investigation. Understanding their structural response is crucial for developing reliable design guidelines and improving their implementation in practical applications.

Extensive research has been conducted on GFRP-RC columns, primarily focusing on the influence of reinforcement configurations, including the role of longitudinal and transverse reinforcement. However, key discrepancies exist in the reported contribution of GFRP longitudinal bars to column capacity. De Luca et al. [1] tested full-scale square GFRP-RC columns under axial loading and reported that GFRP bars contributed less than 5% to the total column capacity, significantly lower than the 12% contribution observed in steel-reinforced columns. They suggested that the compression resistance of GFRP bars could be neglected. In contrast, Tobbi et

al. [2] conducted similar tests on square GFRP-RC columns and found that GFRP bars contributed up to 10% of the total load capacity—comparable to steel’s 12% contribution—highlighting inconsistencies in prior assessments. Similarly, Afifi et al. [3] observed that GFRP and steel-reinforced columns exhibited comparable axial behavior. The contribution of longitudinal GFRP bars ranged from 5% to 10%, and ignoring this contribution resulted in an underestimation of peak load capacity by approximately 35%.

In terms of transverse reinforcement, studies have demonstrated the effectiveness of FRP ties and spirals in confinement. Prachasaree et al. [4] and Tu et al. [5] reported that GFRP spirals provided superior confinement and deformability compared to conventional ties. Tobbi [6] observed that FRP ties significantly enhanced concrete strength and ductility in square GFRP-RC columns, with closed ties performing better than C-shaped ties. While numerous studies [7–12] have examined circular spirals for their confinement efficiency, research on square spirals—particularly in slender GFRP-RC columns—remains scarce. Given that square columns are widely used in practice, the role of GFRP square spirals as a continuous transverse reinforcement system requires further investigation.

The behavior of slender GFRP-RC columns differs significantly from that of short columns due to the pronounced influence of second-order effects, reduced stiffness, and increased susceptibility to instability and global buckling. As slenderness increases, the interaction between axial and bending effects becomes more critical, leading to greater deformations and potential reductions in load-carrying capacity. However, research on slender GFRP-RC columns remains limited due to complex experimental setups, challenges in achieving realistic boundary conditions, and the need for advanced numerical modeling techniques to accurately capture their nonlinear response. Addressing these gaps is essential for developing reliable design guidelines and improving the

structural performance of slender GFRP-RC columns in practical applications. Previous studies have proposed different slenderness limits for GFRP-RC columns. Mirmiran et al. [13] suggested reducing the slenderness limit from 22 (for steel-RC) to 17 for GFRP-RC columns with a 1% reinforcement ratio. Jawaheri Zadeh and Nanni [14] recommended slenderness limits of 14 and 19 for rectangular columns reinforced with GFRP and CFRP bars, respectively. Abdelazim et al. [15] further refined these limits through experimental and analytical studies. Khorramian et al. [16] proposed a reliability-based approach to optimize slenderness limit expressions for GFRP-RC columns. They found the ACI 440 [17] expression had a reliability index of 3.99–4.53 and suggested alternative equations to achieve target indices of 4.0–4.5. However, existing studies have not addressed the role of square spirals in slender GFRP-RC columns under eccentric loading.

Given the inevitable occurrence of eccentricity in axial loads, the impact of eccentricity on FRP-reinforced concrete columns is a topic of discussion. Some researchers argue for disregarding the contribution of FRP bars under eccentric loading [18–20], whereas others contend that it should not be overlooked [7,21–23]. Hales et al. [24] showed using steel longitudinal bars increased axial load capacity by 37% compared to GFRP bars, while GFRP-RC columns exhibited 26% more lateral deflection due to their elastic properties. Xue et al. [25] showed that including GFRP bars' compression contribution led to more accurate predictions of the behavior of slender rectangular GFRP-RC columns under compressive load. Khorramian and Sadeghian [26] observed that eccentrically loaded GFRP-RC columns failed due to spalling and crushing of concrete, with no bar crushing or buckling. They found that higher eccentricity raised the GFRP bars' strain at peak load, highlighting that the bars' contribution depends on their modulus and ultimate strain level. Khorramian and Sadeghian [27] observed that slender GFRP-RC columns sustained a nearly constant load after concrete spalling/crushing until GFRP bar failure, allowing for increased

moment capacity despite significant lateral displacement. Guérin et al. [23] tested full-scale GFRP-RC columns, finding that bar rupture on the tension side was not the failure mode under large eccentric loading, and increasing reinforcement ratios boosted strength by 35%. In another study by Guérin et al. [28], square GFRP-RC columns with GFRP ties tested under various eccentricity levels. The GFRP-RC columns exhibited similar behavior to steel-RC columns, with eccentricity significantly impacting strength and failure modes. Hadi et al. [29] found GFRP-reinforced high-strength concrete (RHSC) columns performed comparably to steel-reinforced columns under concentric loading but had 12% lower capacity under a 50-mm eccentric load. Similarly, Hasan et al. [30] observed a 10-12% capacity reduction under eccentric loading. Hadi et al. [19] reported that GFRP-RC columns had 4.8% lower concentric and 18.5% lower eccentric capacity than steel-reinforced columns, with sudden, brittle failures and reduced ductility.

Despite previous studies on GFRP-RC columns, the structural role of GFRP square spirals in slender columns under concentric and eccentric loading remains largely unexplored. Existing research has primarily focused on the use of discrete ties as transverse reinforcement in square columns, overlooking the potential advantages of square spirals, which offer a more integrated and efficient reinforcement system—similar to how circular spirals outperform hoops in confinement efficiency. This study addresses this critical gap by investigating the influence of slenderness and load eccentricity on the behavior of square GFRP-RC columns reinforced with square spirals. The novelty of this research lies in its systematic examination of GFRP square spirals in slender columns, an area that has not been previously studied. Experimental tests are conducted on columns with slenderness ratios of 20, 40, and 60—the latter of which has rarely been tested due to space limitations—under both concentric loading and eccentricities of 15% and 30%. The findings of this study provide new insights into the effectiveness of square spirals in slender GFRP-

RC columns, contributing to the advancement of durable and corrosion-resistant structural solutions. An analytical model, validated against experimental results, is developed to predict load-lateral deflection, bar strain, and loading path. Furthermore, this model is used to propose a slenderness limit for these columns, contributing to the broader understanding of their structural behavior and design codes such as ACI CODE-440.11-22 [31] and CSA/CAN S806:12(R21) [32].

2. EXPERIMENTAL PROGRAM

2.1. Specimens Layout

The specimens in this study include nine GFRP-RC columns with square spirals as transverse reinforcement. Each column has a cross-sectional dimension of 203×203 mm with a concrete cover of 25.4 mm. Longitudinal reinforcement consisted of six #5 GFRP bars, while transverse reinforcement used #3 square spirals with a uniform pitch of 50 mm. These spirals provide continuous lateral support along the column height (Fig. 1). Three column lengths (l), 1220 mm, 2440 mm, and 3660 mm were selected to correspond to slenderness ratios (λ) of 20, 40, and 60, respectively. These slenderness ratios cover a practical range commonly observed in the literature, ensuring that the study captures the behavior of slender columns across different levels of slenderness. The columns were subjected to both concentric and eccentric axial loading. Eccentric loading was applied at eccentricities of 15% and 30% of the column's cross-sectional height (h), representing low and moderate eccentricity cases that are typical within the practical range of loading conditions. The specimens are labeled using the format SX-eY, where "S" represents the slenderness ratio, followed by "X," which indicates the specific slenderness ratio value. The letter "e" denotes eccentricity, and "Y" specifies the eccentricity ratio as a percentage of the column's cross-sectional dimension. For example, a specimen labeled S40-e15 corresponds to a column with a slenderness ratio of 40 and a load eccentricity of 15% of the column's cross-section. Table 1

summarizes the detailed properties of the specimens. Fig. 1 illustrates the reinforcement details and specimens' geometries.

Table 1. Test matrix

#	Specimen ID	Length, l (mm)	Slenderness ratio, $\lambda=Kl/r^*$	Eccentricity ratio, e/h^{**}
1	S20-e00	1220	20	0
2	S20-e15	1220	20	15
3	S20-e30	1220	20	30
4	S40-e00	2440	40	0
5	S40-e15	2440	40	15
6	S40-e30	2440	40	30
7	S60-e00	3660	60	0
8	S60-e15	3660	60	15
9	S60-e30	3660	60	30

* K : effective length factor ($K=1$ for pinned-pinned column), l : column length, r : radius of gyration

** e : eccentricity

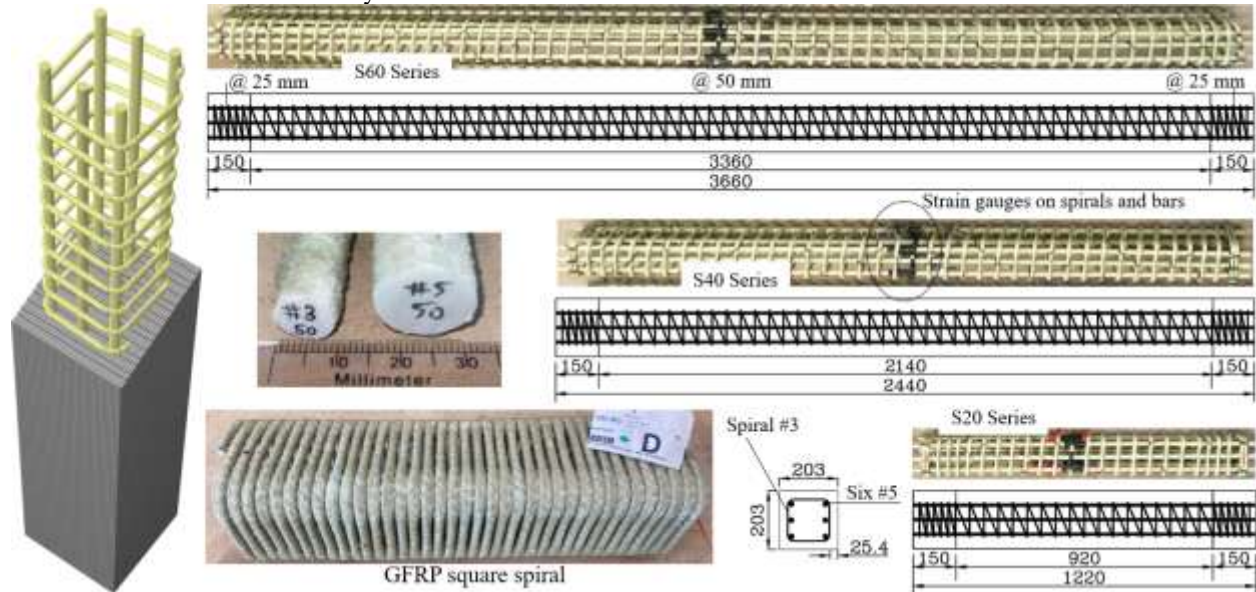


Fig 1. Specimens' reinforcement details and geometry, including the engineering details for the tested columns (All dimensions are in mm)

2.2. Materials

The GFRP bars and spirals, donated by Pultrall Inc., consisted of 85% glass fiber content and were manufactured with vinyl ester resin. Mechanical properties of the straight GFRP bars were determined through tensile testing (Fig. 2) according to ASTM D7205/D7205M [33], conducted on five samples, as well as through compression testing (Fig. 2) using a custom-designed fixture

[34]. The compressive properties of GFRP bars have been the subject of research [35–41] yet no standardized testing method has been established for their comprehensive evaluation. Mechanical properties of the GFRP spirals were obtained from the manufacturer’s catalogue. Table 2 provides a detailed summary of the material properties of the GFRP bars used in this study.

Table 2. GFRP bars material properties

Size	d_b (mm)	f_{ftu} (MPa)	f_{fcu} (MPa)	E_{ft} (GPa)	E_{fc} (GPa)	ϵ_{ftu} ($\mu\text{m/m}$)	ϵ_{fcu} ($\mu\text{m/m}$)
#5*	15.9	1020±25	952±66	53.7±0.1	50.0±0.7	0.021	0.018
#3**	9.5	460		50			

* According to ASTM D7205/D7205M [33], and designed fixture [34].

** Provided by the manufacturer

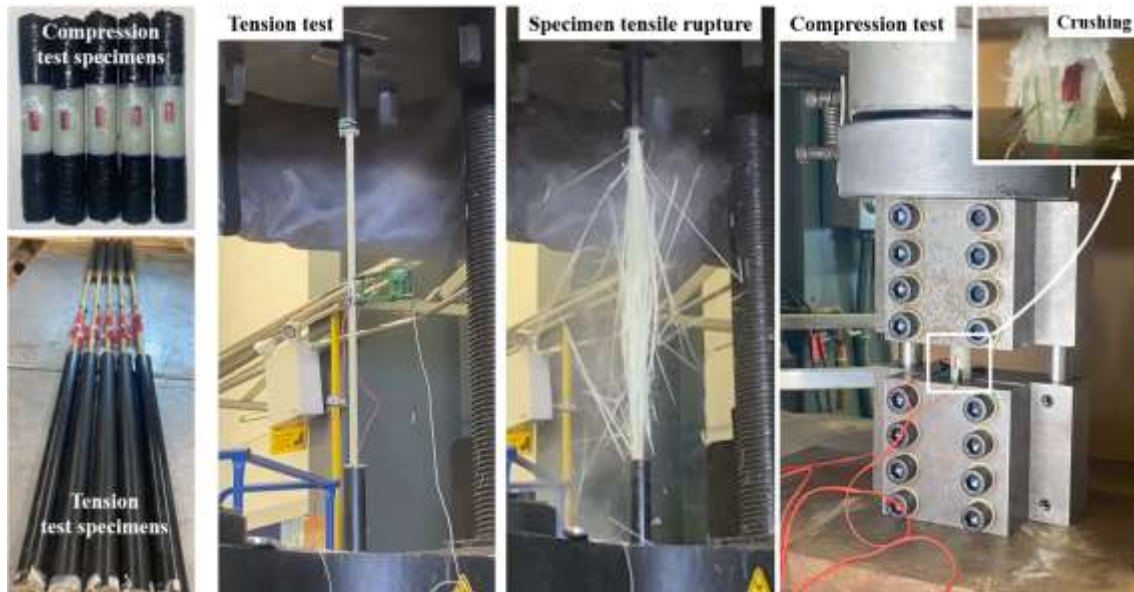


Fig. 2. Tension and compression tests on GFRP bars

The concrete used for specimen fabrication was ready-mix concrete with a maximum aggregate size of 12.5 mm and a slump of 150 mm. The average compressive strength was 32.5 MPa, based on nine standard cylinder tests (100 × 200 mm) cured under the same conditions as the columns. Testing followed ASTM C39/C39M-21 [42], with a standard deviation of 2.0 MPa. The elastic modulus, estimated using ACI CODE-440.11-22 [31], is approximately 26.8 GPa. Figure 3 shows the test cylinders and a tested specimen.

2.3. Preparation of the Specimens

The longitudinal bars were cut to lengths corresponding to each column length, and the spirals were attached to these bars using zip ties. To maintain a consistent spiral pitch of 50 mm along the column length, spacers were used; however, at both column ends, the pitch was reduced to 25 mm over a 150 mm length to prevent premature end failures.

Each specimen was positioned within formwork, with the concrete cover precisely set using wire spacers. Concrete was poured into the formwork and a vibrator was used to compact it every 150 mm along the column height to ensure uniform compaction. Standard concrete cylinders were cast concurrently to monitor material properties. Both the columns and cylinders were cured in the same environment for 28 days under moisture-controlled conditions. Fig. 3 illustrates the specimens preparation process, strain gauging and cylinder tests.



Fig. 3. GFRP-RC specimens preparation process

2.4. Instrumentation and Test Setup

The tests were carried out using the horizontal actuator of a 2 MN capacity MTS hydraulic machine. As shown in Fig. 4, the actuator was set up on the right side of the specimen, while the left end was anchored to a rigid end block. Each specimen was secured using custom end fixtures

with collar plates bolted into place. Grout bags were placed between the specimen and the steel plates to evenly distribute stress and prevent local cracking at the contact points.

Each specimen was internally instrumented with eight strain gauges—four attached to the longitudinal bars and four to the spiral reinforcement at mid-height. The strain gauges were bonded using a high-strength adhesive after proper surface preparation to ensure accurate strain readings. The gauges on the longitudinal bars were aligned with the bar axis, while those on the spirals were placed circumferentially to capture hoop strains. For lateral displacement measurement, two string potentiometers (SPs) were mounted on independent pedestals placed on either side of the specimen at mid-height. The SPs measured displacement relative to a fixed reference point to ensure accurate tracking of lateral deformations.

A displacement-controlled load was applied at a rate of 2.0 mm per minute, with strain and displacement measurements continuously recorded through the data acquisition system. The load was applied via the hydraulic actuator and measured by the actuator's internal load cell. A preloading stage was performed before each test to eliminate any initial gaps in the load path. This was achieved by applying a force-controlled preload of at least 10 kN (or 1% of the expected peak load) over 30 seconds, followed by a 2-minute hold before initiating displacement-controlled loading. Testing continued until the axial load dropped below 20% of the peak load, signaling either sudden or gradual specimen failure.

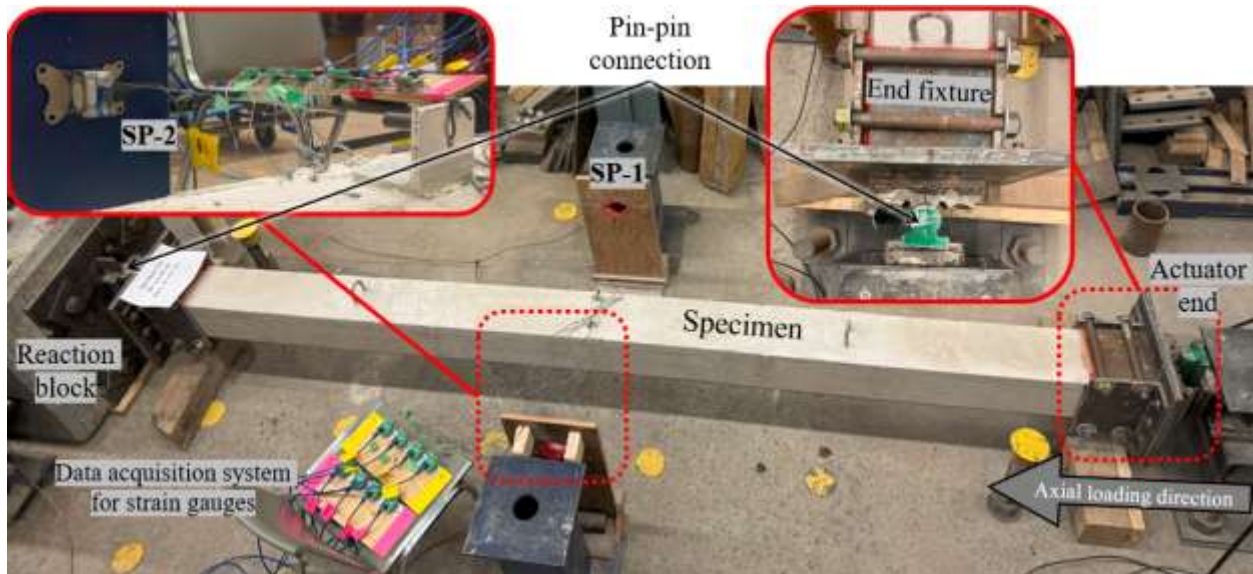


Fig. 4. Test setup and instrumentation

3. TEST RESULTS AND DISCUSSION

The key results of this study are summarized in Table 3. Under concentric loading, the peak load decreased with increasing slenderness ratio due to the greater susceptibility of slender columns to instability and global buckling, even in the absence of significant bending effects. Under eccentric loading, for a given eccentricity ratio, the combined effects of bending and axial forces, along with amplified second-order effects, led to a reduction in the column's ultimate axial strength.

Regarding bar strains, longitudinal bars' compressive strains were comparable under concentric loading with an average of $0.0025 \mu\text{m/m}$. However, under eccentric loading, the compressive strains at peak load decreased with increase of slenderness, primarily due to the reduced peak load and lower stress on the compressive bars. Conversely, tensile strains in the longitudinal bars increased with eccentricity, reflecting the greater contribution of tensile reinforcement under combined bending and axial loading.

The influence of square spirals was assessed by examining their strains. Spiral strains decreased with increasing slenderness at each level of eccentricity. This behavior is likely due to reduced confinement demand under flexural-dominated responses and greater reliance on longitudinal

reinforcement in slender or eccentrically loaded columns. Higher eccentricities and slenderness ratios resulted in lower spiral strains, indicating that square spirals are most effective in enhancing confinement and strength in columns with lower slenderness ratios and minimal load eccentricity. Nonetheless, even at higher slenderness ratios and eccentricities, square spirals contribute to delaying local bar buckling and maintaining the structural integrity of the section.

Table 3. Key test results at peak load

Specimen ID	P_{max} (kN)	$\varepsilon_{fc,0}$ ($\mu\text{m/m}$)	$\varepsilon_{ft,0}$ ($\mu\text{m/m}$)	$\varepsilon_{st,0}$ ($\mu\text{m/m}$)	δ (mm)	M_{max} (kN-m)
S20-e00	1384	-0.0025	–	0.0003	–	–
S40-e00	1167	-0.0028	–	0.0006	–	–
S60-e00	951	-0.0022	–	0.0005	–	–
S20-e15	865	-0.0032	-0.00002	0.0007	5.5	31.1
S40-e15	749	-0.0028	-0.0003	0.0005	15.7	34.6
S60-e15	588	-0.0018	0.0004	0.0002	23.8	31.9
S20-e30	558	-0.0018	0.0018	0.0006	9.6	39.4
S40-e30	393	-0.0017	0.0022	0.00008	25.0	33.3
S60-e30	323	-0.0008	0.0014	0.00001	35.4	31.1

$\varepsilon_{fc,0}$: Strain in bars on the compression side

$\varepsilon_{ft,0}$: Strain in bars on the tension side

$\varepsilon_{st,0}$: Tensile strain in spirals

δ : Mid-height lateral displacement

3.1. Failure Mechanisms

The failure modes are significantly influenced by the level of eccentricity and slenderness. The section is organized into subsections based on load eccentricity, with each subsection presenting and comparing the observations related to varying slenderness.

3.1.1. Concentric Load

An increase in slenderness made the columns more prone to geometric instability, as any lateral deformations amplified the bending moments. Additionally, the inherent asymmetry of the square spiral contributed to this vulnerability. Fig. 5 illustrates the failure modes under concentric loading. The lateral displacement shown in the figure occurred post-failure.

For the specimen with $\lambda = 20$, no global buckling was observed. The longitudinal bars slipped through the concrete and penetrated the end grout bag, likely due to the slightly thicker grout layer

in this specimen. As a result, bar crushing in compression did not occur. However, if bar punching had been restrained, crushing would likely have taken place. This aligns with the findings of Khorramian and Sadeghian [27], who reported that specimens with $\lambda \leq 22$ did not exhibit global buckling. For the specimen with $\lambda = 40$, failure was characterized by bar crushing at peak load and sudden lateral instability. Once the crushing of the bars occurred, the spiral twisted out of plane due to the pressure exerted by the concrete. For the specimen with $\lambda = 60$, similar behavior was observed. All specimens showed transverse cracks around the spirals on the tension side.

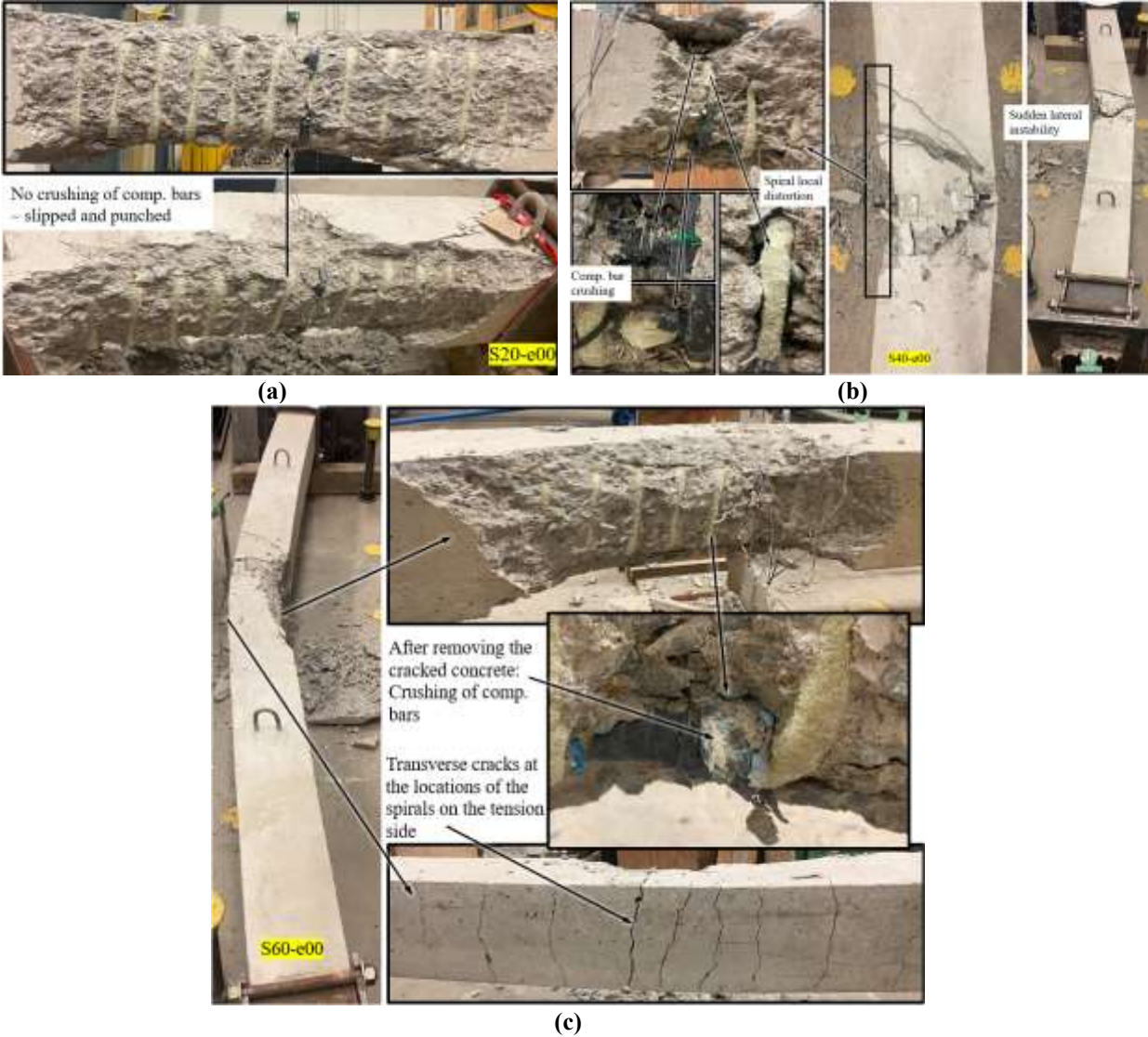


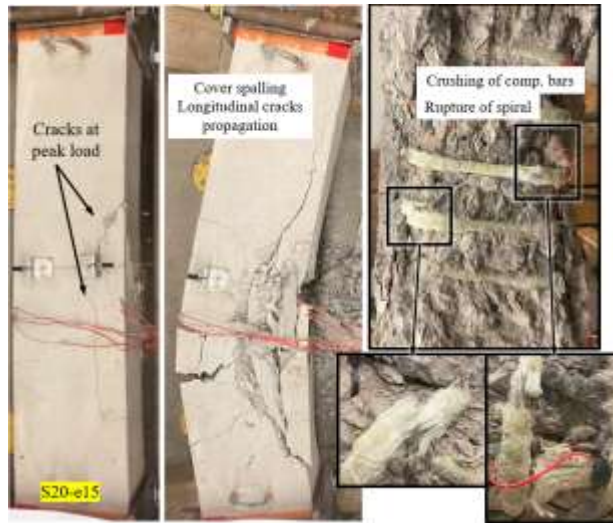
Fig. 5. Failure mods in the specimens under concentric loading: a) $\lambda=20$, b) $\lambda=40$, and c) $\lambda=60$

3.1.2. Low Load Eccentricity ($e=15\%$)

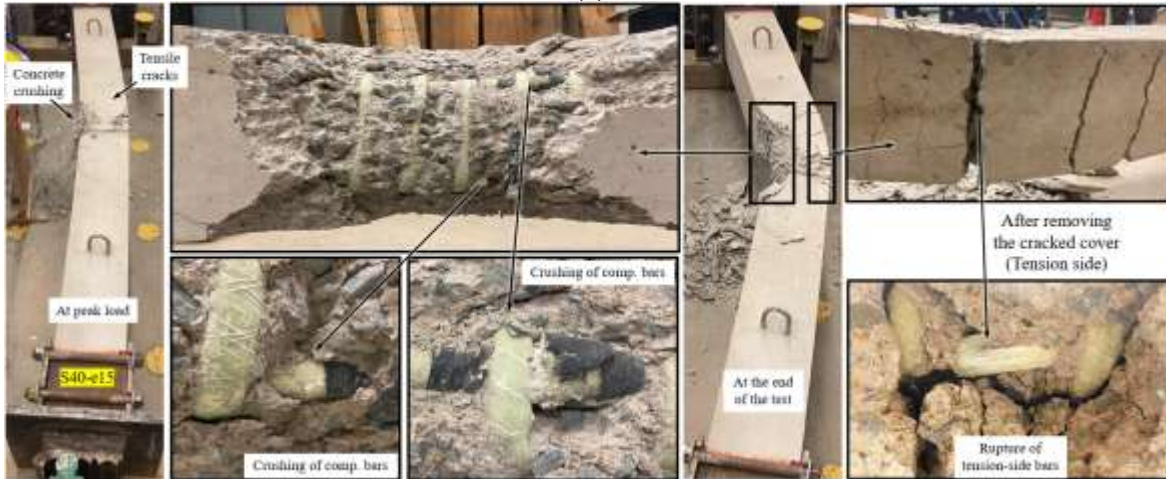
As illustrated in Fig. 6(a), cracks in specimen S20-e15 initiated around the mid-height on the compression side at the peak load and subsequently propagated toward the ends. After further axial displacement beyond the peak load, the specimen failed due to the crushing of the longitudinal bars on the compression side. As the test progressed, additional displacement caused the spiral to rupture at two locations on the compression side, attributed to concrete expansion. On the tension side, the bars slipped during the post-peak phase, preventing tension failure of the bars.

For specimen S40-e15 ($\lambda=40$), cracks began to form near the peak load. At the peak load, sudden concrete spalling was observed on the compression side, as depicted in Fig. 6(b). With increased displacement, spalling progressed, and transverse cracks on the tension side widened. After reaching approximately 2.5 times the peak load displacement, the longitudinal bars on the compression side crushed, causing small concrete fragments to eject. Subsequently, continuous sounds of bar failure were heard, culminating in the rupture of the tension side bars a few seconds later, at which point the test was terminated. The longer embedded length of bars in S40-e15 provided greater anchorage compared to S20-e15, which prevented bar slippage. Consequently, tension failure of the bars occurred post-peak, following the crushing of the compression side bars.

For specimen S60-e15 ($\lambda=60$), as illustrated in Fig. 6(c), cracks began forming near the peak load. At peak load, the concrete cover on the compression side failed silently, accompanied by a sudden lateral movement at mid-height. Concrete spalling continued during the post-peak phase, with larger chunks of the concrete cover detaching as displacement increased. No sound of bar crushing was observed during this phase. Finally, at approximately 6.5 times the peak load displacement, the longitudinal bars on the tension side ruptured, leading to complete failure of the specimen. No crushing of the compression side bars was observed in this specimen.



(a)



(b)



(c)

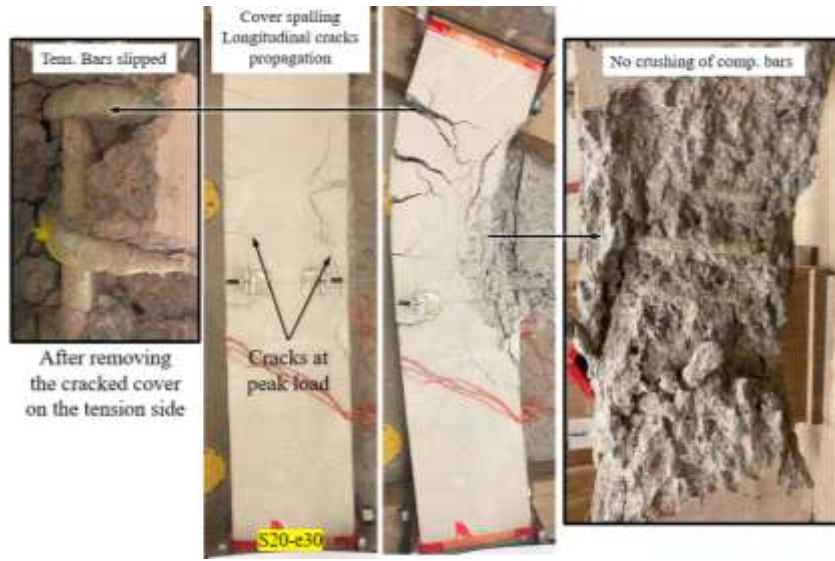
Fig. 6. Failure modes in the specimens under 15% load eccentricity: a) $\lambda=20$, b) $\lambda=40$, and c) $\lambda=60$

3.1.3. Moderate Load Eccentricity ($e=30\%$)

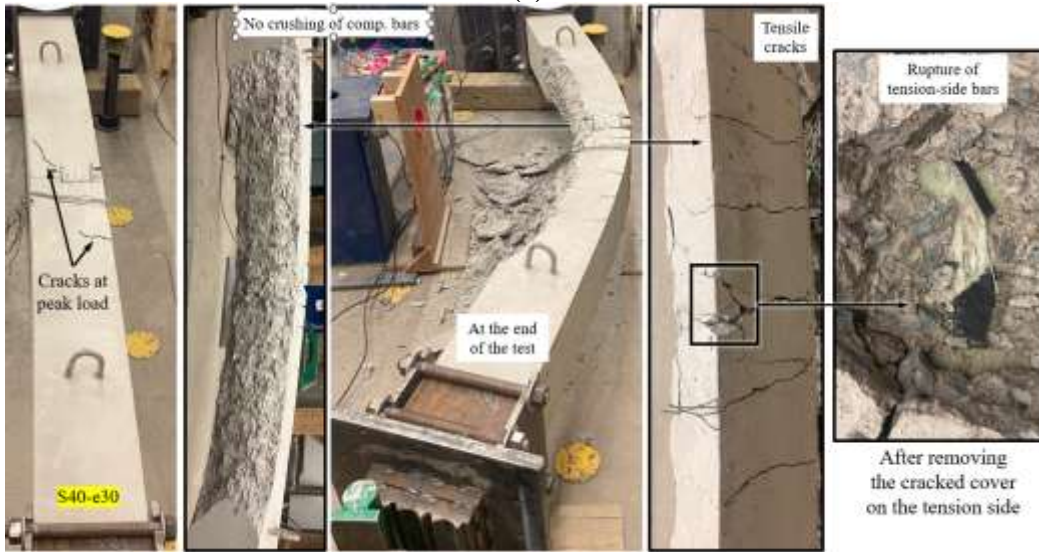
Fig. 7 compares the failure patterns of specimens S20-e30, S40-e30, and S60-e30, under 30% eccentricity ratio. For S20-e30, the load increased steadily until reaching the peak load, accompanied by the formation of cracks on both the compression and tension sides. Compressive cracks appeared around the mid-height and extended longitudinally along the column. The concrete cover on the compression side completely spalled, leading to a load drop to less than 20% of the peak load. As shown in Fig. 7(a), no crushing of the longitudinal bars or spiral failure was observed. During the final stages of loading at high axial displacements, the bars on the tension side slipped through the concrete.

For S40-e30, the peak load was reached when cracks formed on the compression side, but no concrete cover spalling was observed at this stage. As displacement increased, larger longitudinal cracks developed along the cover, followed by partial cover detachment and a secondary drop in load. This was not accompanied by audible bar failure. After reaching approximately 5.5 times the peak load displacement, the tension side bars failed. No crushing of the compression side bars was observed, as shown in Fig. 7(b).

Specimen S60-e30 exhibited behavior similar to that of S40-e30. Cracks were observed on both the compression and tension sides near the peak load, with tension-side cracks roughly following the spiral pitch pattern. After reaching approximately 11.5 times the peak load displacement, the bars on the tension side failed. As with S40-e30, no crushing of the compression side bars was observed, as shown in Fig. 7(c).



(a)



(b)



(c)

Fig. 7. Failure mods in the specimens under 30% load eccentricity: a) $\lambda=20$, b) $\lambda=40$, and c) $\lambda=60$

The observed failure patterns of the specimens are summarized and categorized based on concrete and reinforcement behavior and overall response in Table 4. As seen, shorter columns ($\lambda = 20$) exhibited axial compression failure with minimal bending effects, while moderate-slenderness ($\lambda = 40$) resulted in a balance of compression and bending-induced failure, depending on eccentricity. Highly slender columns ($\lambda = 60$) failed primarily due to instability and tension-side bar rupture at large displacements. With increasing load eccentricity, failure mechanisms shifted from compression-dominated crushing to bending-induced tension failure as also observed by other researchers [27,28,43].

Table 4. Summary of categorized failure modes for tested GFRP-RC columns

Specimen ID	Concrete Cover	Longitudinal Bars	Spiral	Overall Behavior
S20-e00	Major crushing along length	Bars slipped and punched grout bag	No failure	Gradual cover failure
S40-e00	Localized crushing, sudden lateral instability	Bars crushed on one side	Local distortion	Sudden post-peak instability due to slenderness
S60-e00	Large chunks spalled, sudden lateral instability	Bars crushed on one side	No failure	Abrupt loss of stability due to slenderness
S20-e15	Cracking at peak, longitudinal cracks post-peak	Compression-side bars crushed – tension bar slipped	Spiral ruptured (2 locations)	Bars slipped on tension side, preventing tension failure
S40-e15	Cracks at peak, spalling progressed	Compression-side bars crushed	No failure	Tension-side bars ruptured after repeated bar failure sounds
S60-e15	Silent failure of compression-side cover at peak	No crushing – tension bar rupture	No failure	Sudden lateral movement at mid-height, tension bars failed late
S20-e30	Cracks at mid-height, full cover spalling	No crushing – tension bar slipped	No failure	Sharp load drop, tension bars slipped at high displacement
S40-e30	Cracks at peak	No crushing – tension bar rupture	No failure	Tension bars ruptured well after peak load
S60-e30	Cracks at peak	No crushing – tension bar rupture	No failure	Tension bars ruptured well after peak load

3.2. Axial Load-displacement

As shown in Fig. 8, under concentric loading, the peak load of S20-e00 (1384 kN) was higher than those of S40-e00 (1167 kN) and S60-e00 (951 kN), demonstrating a decreasing trend with increasing slenderness. Post-peak, S40-e00 and S60-e00 experienced rapid load drops due to their higher susceptibility to instability, with brittle failure dominated by concrete crushing and longitudinal bar buckling. In contrast, S20-e00 maintained a residual load capacity of

approximately 1200 kN for about 4 mm of axial deformation, as the spirals effectively confined the core. This post-peak behavior aligns with the observations of Abdelazim et al. [44] on circular spirals at slenderness ratios below 23. However, more slender columns exhibited sudden instability due to a combination of factors, including non-symmetric spiral deformations, minor accidental eccentricities, and gradual loss of column straightness as the concrete cover crushed. Additionally, longer columns developed greater bending moments under high axial loads, accelerating failure and contributing to the observed abrupt load drops.

With increased load eccentricity, peak axial loads dropped significantly. At e15, the influence of slenderness became more pronounced, with S20-e15 reaching a higher peak load (845 kN) than S40-e15 (749 kN) and S60-e15 (588 kN). This trend indicates that slender columns experienced greater reductions in capacity due to excessive second-order moments. At e30, the combined effects of slenderness and bending further reduced capacity, with S60-e30 exhibiting the lowest peak load (323 kN). These results highlight that while slenderness alone affects load capacity, its impact becomes more pronounced when combined with bending at higher eccentricities. Similar observations were reported by Khorramian and Sadeghian [27] for square slender columns with ties. Under eccentric loading, the sudden load drops after peak capacity were attributed to concrete crushing on the compression side. However, despite this initial failure, the columns retained a residual load capacity of approximately 30–40% of their peak load at 15% eccentricity and around 50% at 30% eccentricity.

Failure modes shifted with increasing eccentricity. Higher tensile strains in the longitudinal bars led to tension failure at large displacements, approximately 8 to 10 times the axial displacement at peak load. The inset box in Fig. 8 illustrates this progression, demonstrating that tension failure became more dominant as eccentricity increased.

Slenderness significantly influenced post-peak behavior. Higher slenderness ratios (S40 and S60) exhibited greater deformations after peak load due to a transition toward tensile failure. These effects were most pronounced under moderate eccentricity (e30), where bending moments governed the response.

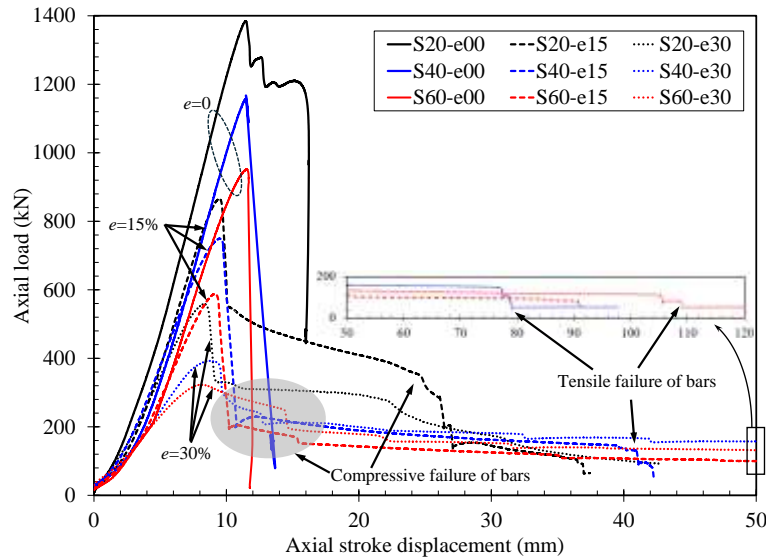


Fig. 8. Axial compressive load versus recorded stroke displacement

3.3. Lateral displacement

Fig. 9 presents the axial load versus mid-height lateral displacement for eccentrically loaded columns with varying slenderness ratios. Columns with lower slenderness (S20) exhibited smaller lateral displacements at peak load. For instance, S20-e15 retained approximately 60% of its peak load after the initial drop, whereas more slender columns, such as S40-e15 and S60-e15, experienced abrupt post-peak load drops to around 30% of their peak load. At higher eccentricities (e30), the failure mechanism transitioned from axial crushing to bending-dominated failure, leading to more gradual load declines in slender columns. However, highly slender columns like S60-e30 still exhibited abrupt load reductions after peak load due to amplified second-order effects and the reduced confinement effectiveness of square spirals. In contrast, S20-e30 maintained a steadier post-peak decline, sustaining about 50% of its first load drop for approximately 40 mm of

lateral displacement, demonstrating the effectiveness of its spirals in mitigating instability under combined axial and bending loads.

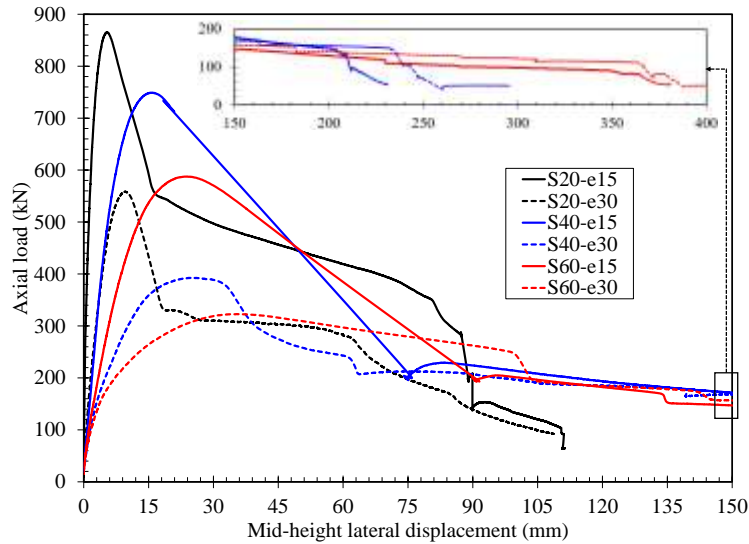


Fig. 9. Axial compressive load versus lateral displacement for eccentrically loaded specimens

3.4. Reinforcement Strain

3.4.1. Longitudinal bars

The axial load-strain behavior of the longitudinal reinforcement is presented in Fig. 10. Under concentric loading, the bars experienced an average compressive strain of $-0.0025 \mu\text{m}/\text{m}$ at peak load, with the strain in column S20-e00 reaching $-0.007 \mu\text{m}/\text{m}$ before failure. As eccentricity increased, the peak compressive strain in the bars decreased, while tensile strain increased due to the transition from axial to bending-dominated behavior. The compressive stress magnitude decreased by approximately 70%, 60%, and 40% when shifting from concentric loading to 30% eccentricity.

Furthermore, at a given eccentricity, an increase in slenderness generally led to a reduction in compressive strain at peak load. For instance, the compressive stress magnitude decreased by 45% and 55% from S20 to S60 at 15% and 30% eccentricity, respectively. However, tensile strain increased significantly, consistent with the observations of Guérin et al. [28]. The maximum

recorded strains at peak load were not necessarily indicative of bar failure, as some strain gauges malfunctioned or detached. For example, under 30% eccentricity, none of the compression-side bars failed. In the case of S60-e30, a slightly lower tensile strain was recorded compared to S40-e30, likely due to early instability and reduced effective load-carrying capacity at higher slenderness ratios. Beyond a certain slenderness limit, strain distribution deviates from expected trends as global instability dominates over material-level strain development. A similar trend was reported by Khorramian and Sadeghian [27], where tensile strain did not consistently increase with slenderness ratio.

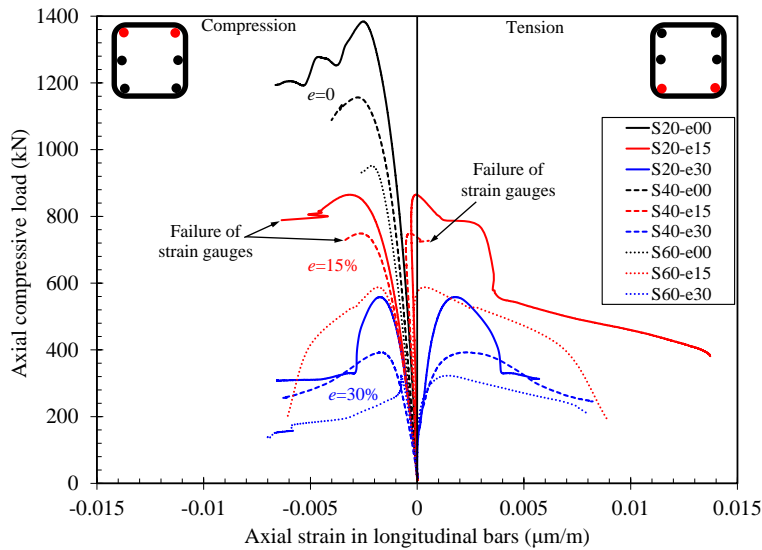


Fig. 10. Axial compressive load versus longitudinal bars axial strain

3.4.2. Transverse reinforcement Strain

Fig. 11 illustrates the tensile strain behavior of the square spirals under different loading conditions. Under concentric loading, the tensile strain in the spirals increased with slenderness, indicating that the spirals deformed more as they confined the concrete core and contributed to maintaining column integrity. However, under eccentric loading, the trend differed significantly. At 15% eccentricity, the average tensile strain in the spirals decreased by approximately 70% as slenderness increased from 20 to 60. At 30% eccentricity, the spiral strain in S60 dropped to about

2% of that in S20, demonstrating a substantial reduction in the effectiveness of spirals with increasing slenderness. A similar reduction in tie strains with increasing load eccentricity was observed by Guérin et al. [28].

Although higher load eccentricity generally increased spiral strains due to greater bending moments, the influence of slenderness was more pronounced. In low-slenderness columns, square spirals provided effective post-peak confinement, helping to maintain load resistance after peak load. However, in more slender columns, their confinement effect was significantly diminished under eccentric loading. Additionally, their post-peak confinement contribution under concentric loading weakened with increasing slenderness, indicating a limited role in stability for slender columns.

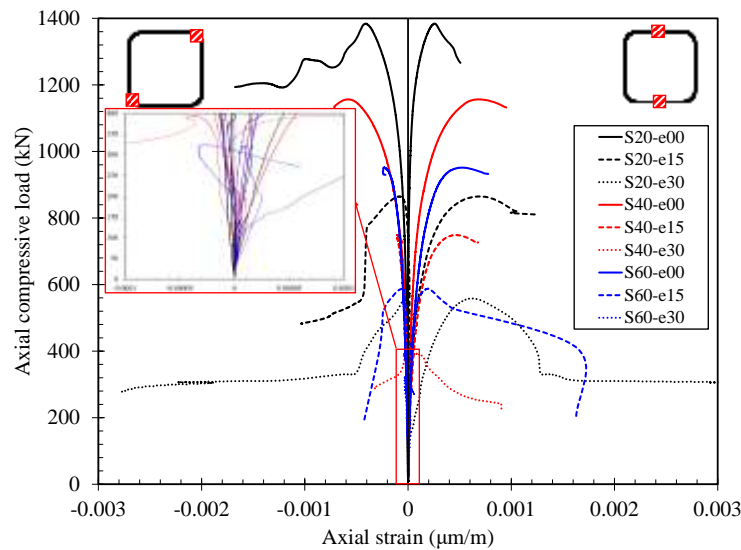


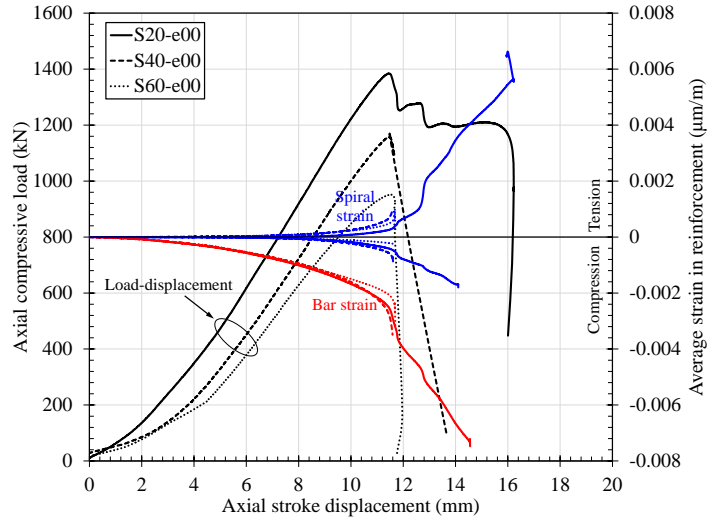
Fig. 11. Axial compressive load versus spiral strain

3.4.3. Combined Illustration

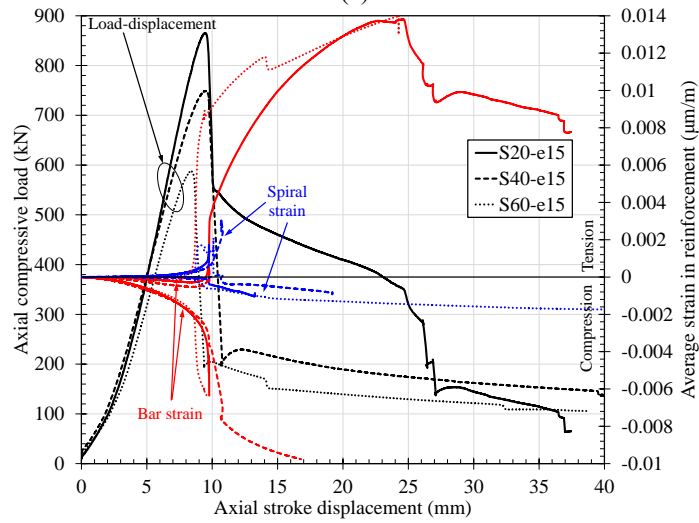
To gain a deeper insight into how strains behave during the load-displacement stages, Fig. 12 is presented. It includes three subfigures, each representing a specific eccentricity level. These subfigures plot axial load, longitudinal bar strain, and spiral strain against axial stroke displacement for all three slenderness ratios, offering a comprehensive view of spiral performance.

Under concentric loading, Fig. 12(a), spiral strains remained symmetrical on the sides and corners up to the peak load, reflecting the symmetry of the applied load. After the peak, only the S20 column exhibited gradual failure due to effective confinement from the spirals. In contrast, slender columns (S40 and S60) experienced rapid instability, as the spirals could not fully counteract geometric imperfections and instability effects. At 15% eccentricity, Fig. 12(b), the behavior of S20 highlights the role of GFRP bars in post-peak resistance. The tension-side bar strain increased to approximately 0.014 before compression bar failure, after which the strain in tension bars dropped as the load on the opposite side of the moment couple was released. In slender columns, sudden load drops led to abrupt increases in bar strain, reflecting instability. Spiral strain on the sides spiked at peak load, often causing strain gauges to fail, while strain on the corners increased more gradually due to uneven load distribution. Under 30% eccentricity, Fig. 12(c), S20 compression bar strains indicate no significant compression failure occurred, even after the load drop. The very mild increase in spiral strain with greater eccentricity and slenderness suggests a reduced ability of the spirals to confine the concrete core effectively in these cases.

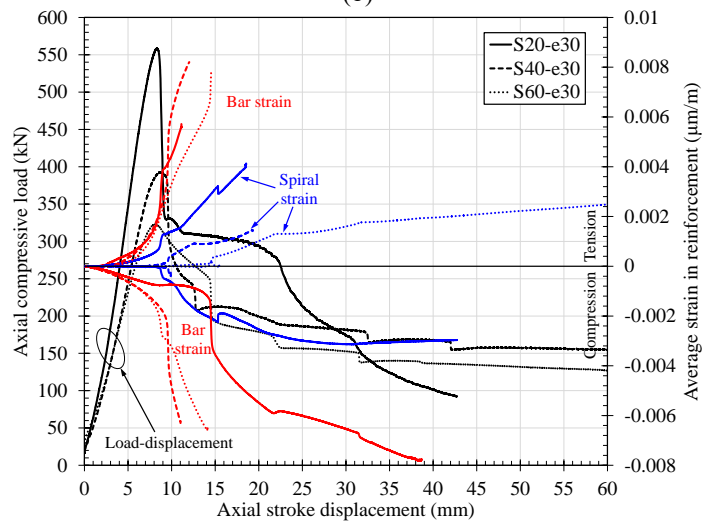
Overall, strain gauges recorded compressive strains up to approximately 0.008, occasionally reaching 0.01, before concrete crushing near mid-height damaged the gauges. These observations highlight the diminishing effectiveness of spirals in slender and highly eccentric columns while indicating their importance in providing stability for shorter columns under moderate loads.



(a)



(b)



(c)

Fig. 12. Axial load and reinforcement strains (bar and spiral) vs. axial stroke displacement: a) Concentric load, b) 15% eccentricity, and c) 30% eccentricity

3.5. Loading Path

As shown in Fig. 13, slenderness significantly influences column behavior. Under concentric loading, slender columns exhibit geometric instability prior to failure, resulting in sudden buckling around mid-height once cracks form. Under eccentric loading, shorter columns, such as S20, display a relatively stable response, with only a 10% and 9% reduction in axial load from the theoretical $P_{max} \times e$. However, increasing slenderness to S40 leads to greater reductions of 20% and 16% for eccentricities of 15% and 30%, respectively. For the slenderest columns, S60, the drops are even more pronounced, reaching 25% and 19%. Shorter columns tend to maintain stability, with bending moments closely aligned with initial eccentricity effects. In contrast, slender columns show significant increases in bending moments beyond $P_{max} \times e$, driven by geometric imperfections and second-order effects. According to the ACI [31], S20 columns with square spirals qualify as slender, consistent with the observed behavior, as the load reductions exceeded the 5% threshold.

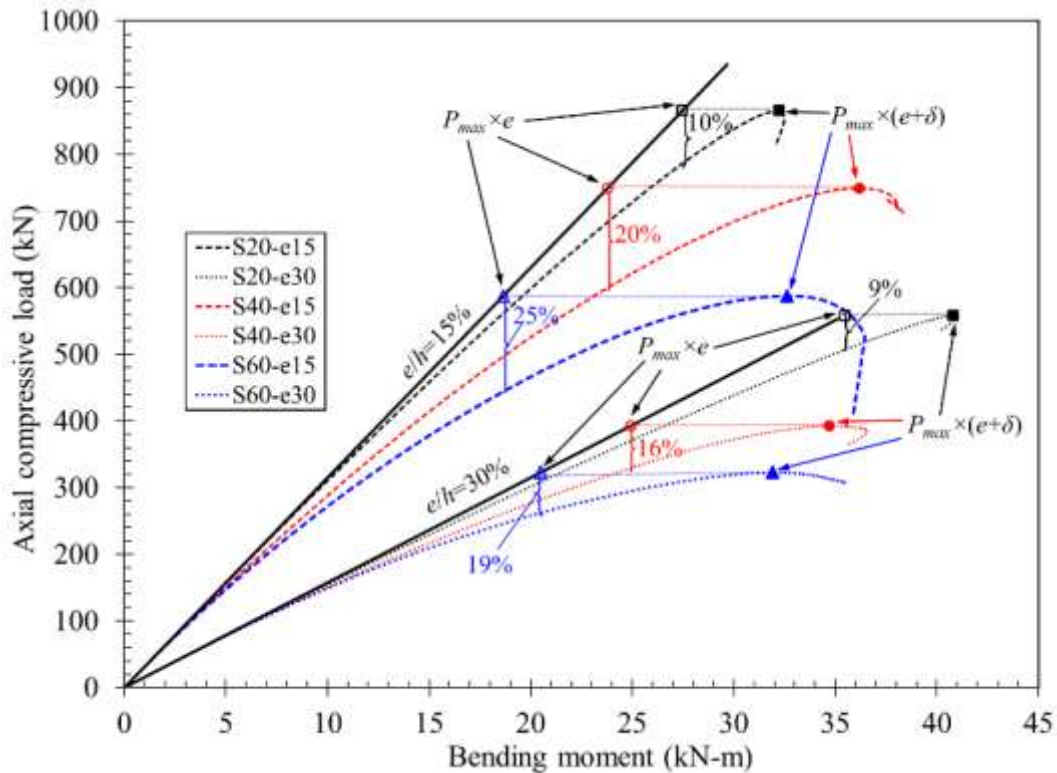


Fig. 13. Loading path

4. ANALYTICAL STUDY

4.1. Model Description

This analytical model performs both section analysis and second-order analysis of GFRP-reinforced concrete (GFRP-RC) columns under varying eccentricities.

The axial force and bending moment capacities are computed based on the column's geometry (dimensions, cover, and bar placement) and material properties. Concrete's elastic modulus, E_c , is calculated as $4700\sqrt{f'_c}$ [31]. Concrete's ultimate strain is taken as $\epsilon_{cu}=0.003$. GFRP bars, with their compressive strength and elastic modulus, contribute to axial and bending resistance, assuming linear elastic behavior until failure. The ultimate strains in tension (f_{fu}) and compression (ϵ_{fcu}) are introduced to the model based on their ultimate strengths and elastic modulus.

The analysis begins with an assumed neutral axis, C_{NA} , at mid-height, refined iteratively based on the difference between the calculated axial force, P_n , and the applied load, P . Strain compatibility determines bar strains, while bar stresses are calculated under linear elastic behavior. Axial and moment contributions from GFRP bars and concrete fibers are summed to achieve equilibrium between forces and moments. Concrete's nonlinear stress-strain relationship is modeled using Popovics' [45] or Thorenfeldt's [46] approach, depending on its strength. Tensile strength and tension stiffening of concrete are neglected for simplicity.

The cross-sectional analysis method is illustrated in Fig. 14. For each load increment, the C_{NA} is adjusted to satisfy equilibrium, where $P_n=F_c+F_f$ (concrete and GFRP contributions), and bending moment ($M_n=M_c+M_f$) is calculated. Interaction diagrams are generated, showing total internal force, P_n , versus total internal moment, M_n , for each load step. The moment-curvature diagrams are prepared for multiple loads, incremented from a minimum load up to the ultimate capacity, by changing the furthest compressive concrete strain.

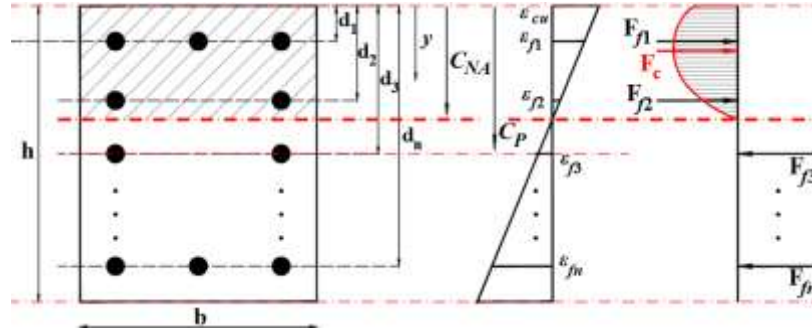


Fig. 14. Cross-sectional analysis

Second-order analysis uses the moment-curvature data from the section analysis. The column's length, L , and initial load eccentricity, e , are specified, and the deflected shape is assumed to follow a sine curve [47]. An iterative process refines the mid-height deflection, starting with initial assumptions at three nodes (mid-height and column ends). For each load increment, the total eccentricity, $e+\delta$, is calculated, where δ represents deflection-induced eccentricity. The corresponding moment, $M_n=P(e+\delta)$, is derived, and curvatures at mid-height, ϕ_m , and the ends, ϕ_0 , are computed using the moment-curvature relationship. The moment-area theorem estimates the deflected shape iteratively until convergence.

After reaching the peak load, the analysis proceeds to the post-peak branch by incrementally reducing the axial load. Curvatures and moments for both the ascending and descending branches are tracked to ensure continuity and capture the ductility and post-peak performance of the column under eccentric loading.

4.2. Verification

The model is validated against experimental results, as shown in Fig. 15, which compares the experimental data with the model predictions. Overall, the model exhibits good agreement with the experimental results. However, at the highest eccentricity and slenderness ratio, the model slightly underpredicts the peak load. This discrepancy is attributed to unexpectedly high test results due to the effect of spirals in these specific case.

Table 5 provides a quantitative comparison of key parameters between the model predictions and test results. The model demonstrates a strong ability to predict peak load accurately. While there are more noticeable differences in initial stiffness, lateral displacement at peak load, and compressive strain at peak load, these variations are expected due to inherent test result variability, idealized modeling assumptions versus real-world imperfections, and the three-dimensional shape of the reinforcement bars, where strain measurements are taken on the surface rather than the centroid.

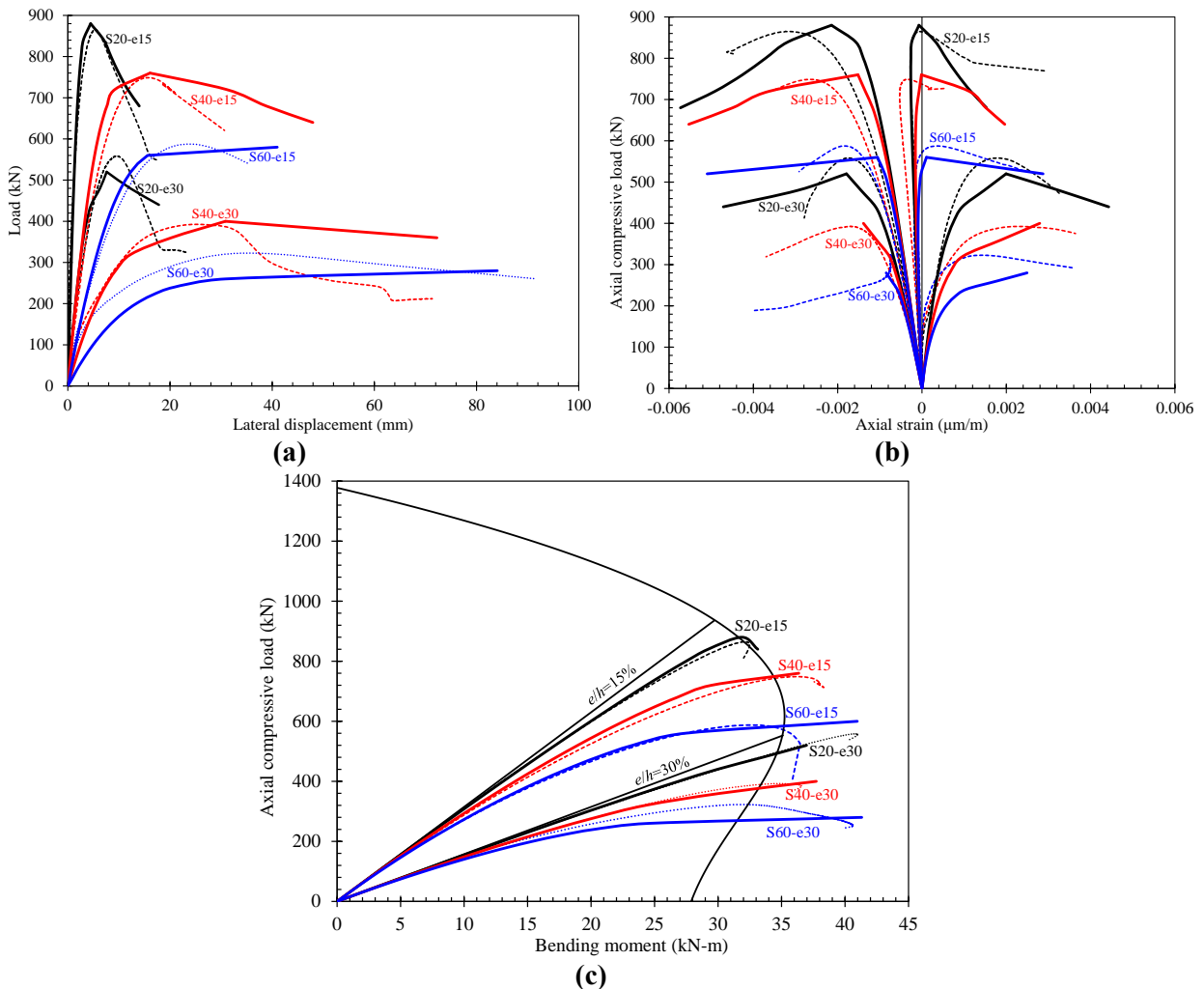


Fig. 15. Comparison of test results (dashed lines) with model predictions (solid lines): a) Load versus lateral displacement, b) Load versus bars axial strain, and c) Loading path

Table 5. Comparison of the key parameters from model predictions and test results

Parameter	λ	e/h	Test	Model	Error (%)	Parameter	λ	e/h	Test	Model	Error (%)
Initial stiffness*	20	0.15	418	410	2%	δ_m (mm)	20	0.15	5.5	4.5	19%
		0.30	95	115	-21%			0.30	9.6	7.6	21%
	40	0.15	94	120	-28%		40	0.15	15.7	16.1	-2%
		0.30	36	35	3%			0.30	25.0	30.8	-23%
	60	0.15	45	55	-22%		60	0.15	23.8	-	-
		0.30	32	20	38%			0.30	35.4	-	-
P_{max} (kN)	20	0.15	865	880	-2%	$\epsilon_{fc,0}$ ($\mu\text{m/m}$)	20	0.15	-0.0032	-0.0021	33%
		0.30	558	520	7%			0.30	-0.0018	-0.0018	0%
	40	0.15	749	760	-1%		40	0.15	-0.0028	-0.0015	46%
		0.30	393	400	-2%			0.30	-0.0017	-0.0014	18%
	60	0.15	588	580	1%		60	0.15	-0.0018	-0.0011	41%
		0.30	323	280	13%			0.30	-0.0008	-0.0008	-6%

* Initial slope of load-deflection diagram between $0.2P_{max}$ and $0.4P_{max}$

5. Slenderness Limit

Fig. 16 illustrates the impact of second-order effects on the loading path of columns, causing it to deviate from the ideal Pe line (dashed line), which represents only first-order effects. The actual loading path intersects the interaction diagram at point A_2 , corresponding to the column's maximum axial load, P_{max} . On the Pe line, the equivalent load level is at point B_1 , with a load reduction of ΔP relative to point B_2 . This reduction, attributed to slenderness effects, varies based on the load eccentricity and the column's slenderness ratio.

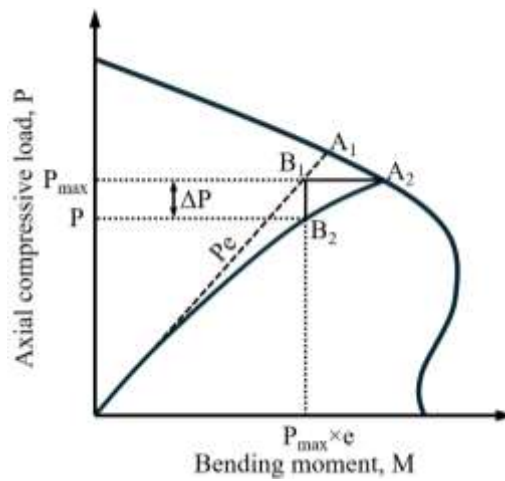


Fig. 16. Slender column's loading path and interaction diagram with ΔP indicating the load reduction due to slenderness effect

The slenderness limit for GFRP-reinforced columns is defined as the slenderness ratio at which the load reduction ΔP equals 5% of P_{\max} [48]. To determine this limit, loading paths were generated for a total of 126 models using the validated analytical model. The models included columns with longitudinal reinforcement ratios of 2%, 3%, and 4%; slenderness ratios of 10, 20, 30, 40, 50, and 60; and load eccentricities of 0.1, 0.12, 0.15, 0.17, 0.2, 0.25, and 0.3. Fig. 17(a) shows the resulting $\Delta P/P_{\max}$ values plotted against the load eccentricity ratio for each slenderness ratio. The data exhibit consistent trends, with higher slenderness ratios resulting in greater $\Delta P/P_{\max}$ values at all eccentricity ratios. Fitted curves are used to extrapolate and predict the reduction at zero eccentricity (concentric loading). As shown in Fig. 17(a), $\Delta P/P_{\max}$ increases progressively with slenderness ratio and eccentricity ratio. This is consistent with the test observations under concentric loading in this study, and the findings of Xue et al. [25] regarding slenderness effects under concentric loading. Subsequently, these values are plotted against the slenderness ratios in Fig. 17(b), with a line fitted to the data points. The slenderness limit is identified as the point where this line intersects $\Delta P/P_{\max}=0.05$ [31], resulting in a slenderness limit of 14, aligns with the limit proposed by Jawaheri Zadeh and Nanni [14].

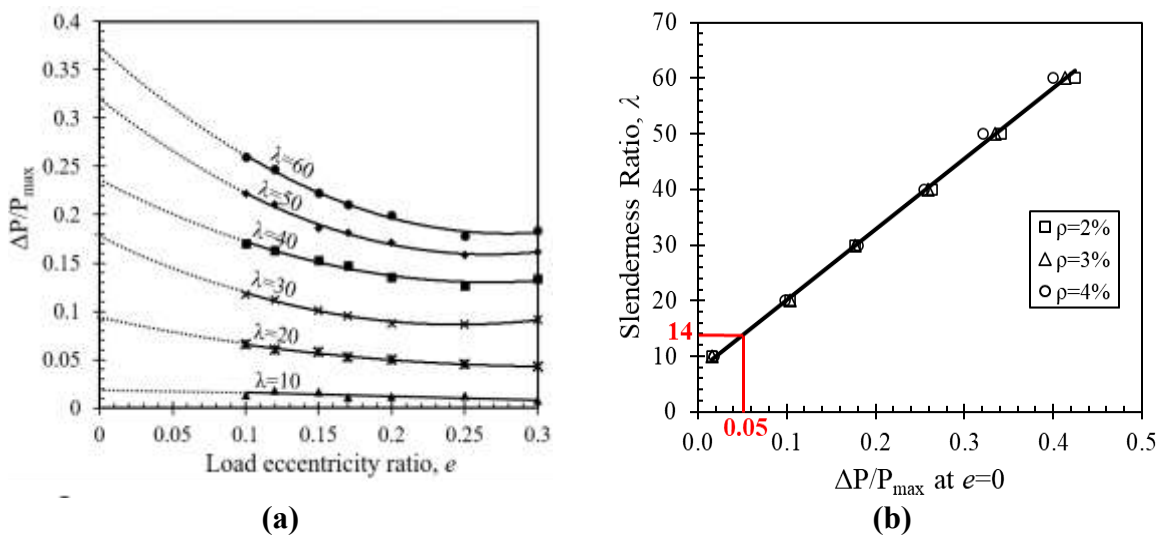


Fig. 17. Relationship between a) load eccentricity and load drop ratio and b) load drop ratio and slenderness ratio

6. LIMITATIONS AND FUTURE DIRECTIONS

Certain limitations in this study suggest opportunities for further exploration. The tests utilized columns with a constant reinforcement pitch of 50 mm and a cross-sectional area of 203×203 mm. Future studies should investigate larger cross-sectional areas and reinforcement patterns to improve the generalizability of the results. The analytical model developed in this study successfully captured the overall behavior of the tested columns but did not explicitly account for the effects of transverse reinforcement, such as spirals. Developing advanced numerical finite element models that incorporate the effects of transverse reinforcement, including variations in spiral pitch, is recommended. These models could provide a more comprehensive understanding of how such reinforcements influence load distribution, confinement, and failure modes.

Comparing numerical finite element models with the analytical model could reveal discrepancies and improve both approaches' predictive capabilities, providing a stronger foundation for designing slender GFRP-reinforced concrete columns in future research.

7. CONCLUSION

This study presents both experimental and analytical investigations into the behavior of slender GFRP-RC columns reinforced with GFRP bars and square spirals. Nine column specimens were tested, covering slenderness ratios of 20, 40, and 60, and load eccentricities of 0%, 15%, and 30% of the section height. The analytical model was validated against the experimental data, and additional analysis was conducted on the slenderness limit of these columns. The key findings are:

- Under concentric loading, an increase in slenderness made the columns more prone to geometric instability due to amplified bending moments caused by lateral deformations. The asymmetry of the square spiral further exacerbated this vulnerability. As a result, the column

strength decreased by 16% and 31% when the slenderness ratio was increased from 20 to 40 and 60, respectively.

- Under eccentric loading, spiral rupture was observed only for a slenderness ratio (λ) of 20 at 15% eccentricity. The strain in the spirals and their contribution to confinement decreased as the slenderness ratio increased. At 15% eccentricity, increasing the slenderness ratio from 20 to 40 resulted in a 13% reduction in load-bearing capacity, while increasing it to 60 led to a 32% reduction. Under 30% eccentricity, these reductions were 30% and 42%, respectively.
- At 15% eccentricity, crushing of the longitudinal bars occurred after the peak load and concrete cover spalling. In contrast, at 30% eccentricity, no crushing of the compression bars or spirals was observed, and tension-side bars failed well after the peak load. This indicates a transition in failure mode from compression-dominated to bending-dominated failure.
- At peak load, the increase of the slenderness ratio decreased the average compressive strain in the bars from approximately 0.0025 to 0.0008, while the average tensile strain increased to about 0.002.
- Square spirals provided confinement to the concrete core under concentric loading, with tensile strain increasing as slenderness increased. However, their effectiveness decreased significantly under eccentric loading, reducing by 70% at 15% eccentricity and to just 2% at 30% eccentricity as the slenderness ratio increased from 20 to 60. While they helped maintain column integrity at a slenderness ratio of 20, their contribution became negligible at slenderness ratios of 40 and 60 under eccentric loading. Additionally, their post-peak confinement effect under concentric loading weakened as slenderness increased.
- The analytical study, based on a sine-shaped deformation assumption for columns under single curvature aligned well with experimental results. Further analytical analyses led to the

recommendation of a slenderness limit of 14 for GFRP-reinforced concrete columns with 2–4% longitudinal reinforcement ratio subjected to single-curvature bending.

- Future studies should investigate larger cross-sectional areas, varying reinforcement ratios, and the influence of different spiral pitches on column behavior. Developing numerical finite element models that account for transverse reinforcement effects is also recommended. Comparing these models with the analytical model could reveal predictive differences and enhance understanding of slender GFRP-reinforced concrete columns.

CRedit Authorship Contribution Statement

A. Sadat Hosseini: Writing – original draft, Methodology, Investigation, Conceptualization, Validation. **P. Sadeghian:** Writing – review & editing, Supervision, Methodology, Funding acquisition, Conceptualization, Resources.

ACKNOWLEDGEMENTS

The authors thank the Natural Sciences and Engineering Research Council of Canada (NSERC) for funding, PULTRALL Inc. for providing V-ROD bars and spirals, and lab technicians Jordan Maerz and Jesse Keane for their essential support with the experimental setup and testing.

DATA AVAILABILITY STATEMENT

The data will be provided upon reasonable request.

REFERENCES

- [1] De Luca A, Matta F, Nanni A. Behavior of full-scale glass fiber-reinforced polymer reinforced concrete columns under axial load. *ACI Struct J* 2010;107:589.
- [2] Tobbi H, Farghaly AS, Benmokrane B. Concrete Columns Reinforced Longitudinally and Transversally with Glass Fiber-Reinforced Polymer Bars. *ACI Struct J* 2012;109.
- [3] Afifi MZ, Mohamed HM, Benmokrane B. Axial capacity of circular concrete columns reinforced with GFRP bars and spirals. *Journal of Composites for Construction* 2014;18:04013017.
- [4] Prachasaree W, Piriyaakootorn S, Sangsrijun A, Limkatanyu S. Behavior and performance of GFRP reinforced concrete columns with various types of stirrups. *Int J Polym Sci* 2015;2015:237231.

- [5] Tu J, Gao K, He L, Li X. Experimental study on the axial compression performance of GFRP-reinforced concrete square columns. *Advances in Structural Engineering* 2019;22:1554–65.
- [6] Tobbi H, Farghaly AS, Benmokrane B. Strength model for concrete columns reinforced with fiber-reinforced polymer bars and ties. *ACI Struct J* 2014;111:789–98.
- [7] Hadi MNS, Karim H, Sheikh MN. Experimental investigations on circular concrete columns reinforced with GFRP bars and helices under different loading conditions. *Journal of Composites for Construction* 2016;20:04016009.
- [8] Hadhood A, Mohamed HM, Ghrib F, Benmokrane B. Efficiency of glass fiber-reinforced polymer (GFRP) discrete hoops and bars in concrete columns under combined axial and flexural loads. *Compos B Eng* 2017;114:223–36.
- [9] Gouda MG, Mohamed HM, Manalo AC, Benmokrane B. Experimental investigation of concentrically and eccentrically loaded circular hollow concrete columns reinforced with GFRP bars and spirals. *Eng Struct* 2023;277:115442.
- [10] Selmy YM, El-Salakawy EF. Behaviour of circular concrete bridge columns internally reinforced with GFRP under reversed-cyclic loading including torsion. *Structures*, vol. 59, Elsevier; 2024, p. 105680.
- [11] Hu XB, Nie XF, Wang JJ, Zhang SS. Behavior of FRP spiral-confined concrete under concentric compression. *Eng Struct* 2024;321:118898.
- [12] Hu XB, Nie XF, Wang JJ, Yu T, Zhang SS. Experimental study on GFRP spiral-confined concrete under eccentric compression. *Compos Struct* 2025;354:118793.
- [13] Mirmiran A, Yuan W, Chen X. Design for slenderness in concrete columns internally reinforced with fiber-reinforced polymer bars. *Structural Journal* 2001;98:116–25.
- [14] Jawaheri Zadeh H, Nanni A. Flexural stiffness and second-order effects in fiber-reinforced polymer-reinforced concrete frames. *ACI Struct J* 2017;114:533.
- [15] Abdelazim W, Mohamed HM, Afifi MZ, Benmokrane B. Proposed slenderness limit for glass fiber-reinforced polymer-reinforced concrete columns based on experiments and buckling analysis. *ACI Struct J* 2020;117:241–54.
- [16] Khorrarnian K, Sadeghian P, Oudah F. Slenderness limit for glass fiber-reinforced polymer reinforced concrete columns: reliability-based approach. *ACI Struct J* 2022;119:249–62.
- [17] ACI. ACI PRC-440.1R-15: Guide for the Design and Construction of Structural Concrete Reinforced with FRP Bars. Farmington Hills, MI: American Concrete Institute; 2015.
- [18] Elchalakani M, Ma G. Tests of glass fibre reinforced polymer rectangular concrete columns subjected to concentric and eccentric axial loading. *Eng Struct* 2017;151:93–104.
- [19] Hadi MNS, Youssef J. Experimental investigation of GFRP-reinforced and GFRP-encased square concrete specimens under axial and eccentric load, and four-point bending test. *Journal of Composites for Construction* 2016;20:04016020.
- [20] Youssef J, Hadi MNS. Axial load-bending moment diagrams of GFRP reinforced columns and GFRP encased square columns. *Constr Build Mater* 2017;135:550–64.

- [21] Hadhood A, Mohamed HM, Benmokrane B. Axial load–moment interaction diagram of circular concrete columns reinforced with CFRP bars and spirals: Experimental and theoretical investigations. *Journal of Composites for Construction* 2017;21:04016092.
- [22] Sun L, Wei M, Zhang N. Experimental study on the behavior of GFRP reinforced concrete columns under eccentric axial load. *Constr Build Mater* 2017;152:214–25.
- [23] Guérin M, Mohamed HM, Benmokrane B, Shield CK, Nanni A. Effect of Glass Fiber-Reinforced Polymer Reinforcement Ratio on Axial-Flexural Strength of Reinforced Concrete Columns. *ACI Struct J* 2018;115.
- [24] Hales TA, Pantelides CP, Reaveley LD. Analytical buckling model for slender FRP-reinforced concrete columns. *Compos Struct* 2017;176:33–42.
- [25] Xue W, Peng F, Fang Z. Behavior and Design of Slender Rectangular Concrete Columns Longitudinally Reinforced with Fiber-Reinforced Polymer Bars. *ACI Struct J* 2018;115.
- [26] Khorramian K, Sadeghian P. Experimental and analytical behavior of short concrete columns reinforced with GFRP bars under eccentric loading. *Eng Struct* 2017;151:761–73.
<https://doi.org/https://doi.org/10.1016/j.engstruct.2017.08.064>.
- [27] Khorramian K, Sadeghian P. Experimental investigation of short and slender rectangular concrete columns reinforced with GFRP bars under eccentric axial loads. *Journal of Composites for Construction* 2020;24:04020072.
- [28] Guérin M, Mohamed HM, Benmokrane B, Nanni A, Shield CK. Eccentric Behavior of Full-Scale Reinforced Concrete Columns with Glass Fiber-Reinforced Polymer Bars and Ties. *ACI Struct J* 2018;115.
- [29] Hadi MNS, Hasan HA, Sheikh MN. Experimental investigation of circular high-strength concrete columns reinforced with glass fiber-reinforced polymer bars and helices under different loading conditions. *Journal of Composites for Construction* 2017;21:04017005.
- [30] Hasan HA, Sheikh MN, Hadi MNS. Performance evaluation of high strength concrete and steel fibre high strength concrete columns reinforced with GFRP bars and helices. *Constr Build Mater* 2017;134:297–310.
- [31] ACI. ACI CODE-440.11-22: Building Code Requirements for Structural Concrete Reinforced with Glass Fiber-Reinforced Polymer (GFRP) Bars-Code and Commentary. American Concrete Institute; 2022.
- [32] CSA. S806:12(R21) - Design and construction of building structures with fibre-reinforced polymers. Canadian Standards Association; 2021.
- [33] ASTM. ASTM D7205/D7205M, Standard Test Method for Tensile Properties of Fiber-Reinforced Polymer Matrix Composite Bars. 2021.
- [34] Sadat Hosseini A, Sadeghian P. Assessing Compressive Properties of GFRP Bars: Novel Test Fixture and Statistical Analysis. *Journal of Composites for Construction* 2025;29:04025011.
- [35] Fillmore B, Sadeghian P. Contribution of longitudinal glass fiber-reinforced polymer bars in concrete cylinders under axial compression. *Canadian Journal of Civil Engineering* 2018;45:458–68.

- [36] Khorramian K, Sadeghian P. Material characterization of GFRP bars in compression using a new test method. *J Test Eval* 2019.
- [37] AlAjarmeh OS, Manalo AC, Benmokrane B, Vijay P V, Ferdous W, Mendis P. Novel testing and characterization of GFRP bars in compression. *Constr Build Mater* 2019;225:1112–26.
- [38] D’Antino T, Pisani MA. Tensile and compressive behavior of thermoset and thermoplastic GFRP bars. *Constr Build Mater* 2023;366:130104.
- [39] Mirdarsoltany M, Roghani H, Masoule MST, Khodadadi N, Ghahremaninezhad A, Nanni A. Evaluating GFRP bars under axial compression and quantifying load-damage correlation. *Constr Build Mater* 2023;409:133945.
- [40] Bujotzek L, Beck D, Apostolidi E, Waldmann D. Experimental and statistical investigations of the material properties of FRP reinforcement in compression. *Constr Build Mater* 2024;414:134782.
- [41] Sadat Hosseini A, Velkumar SK, Sadeghian P. Behavior of GFRP-Reinforced Concrete Members under Combined Bending Moment and Low Axial Load. *Journal of Composites for Construction* 2024;28:04024025.
- [42] ASTM. ASTM C39 / C39M, Standard Test Method for Compressive Strength of Cylindrical Concrete Specimens. 2021.
- [43] Salah-Eldin A, Mohamed HM, Benmokrane B. Effect of GFRP reinforcement ratio on the strength and effective stiffness of high-strength concrete columns: Experimental and analytical study. *Journal of Composites for Construction* 2020;24:04020055.
- [44] Abdelazim W, Mohamed HM, Benmokrane B. Inelastic second-order analysis for slender GFRP-reinforced concrete columns: Experimental investigations and theoretical study. *Journal of Composites for Construction* 2020;24:04020016.
- [45] Popovics S. A numerical approach to the complete stress-strain curve of concrete. *Cem Concr Res* 1973;3:583–99.
- [46] Thorenfeldt E. Mechanical properties of high-strength concrete and applications in design. *Symposium Proceedings, Utilization of High-Strength Concrete, Norway, 1987, 1987.*
- [47] James K. Wight. *Reinforced Concrete: Mechanics and Design*. Seventh Edition. Pearson; 2015.
- [48] MacGregor JG, Wight JK, Teng S, Irawan P. *Reinforced concrete: Mechanics and design*. vol. 3. Prentice Hall Upper Saddle River, NJ; 1997.